Hierarchical mesoporous perovskite $La_{0.5}Sr_{0.5}CoO_{2.91}$ nanowires with ultrahigh capacity for Li-air batteries

Yunlong Zhao[1], Lin Xu[1], Liqiang Mai[2], Chunhua Han, Qinyou An, Xu Xu, Xue Liu, and Qingjie Zhang

State Key Laboratory of Advanced Technology for Materials Synthesis and Processing, Wuhan University of Technology, Wuhan 430070, China

Edited* by Charles M. Lieber, Harvard University, Cambridge, MA, and approved October 10, 2012 (received for review June 18, 2012)

Lithium-air batteries have captured worldwide attention due to their highest energy density among the chemical batteries. To provide continuous oxygen channels, here, we synthesized hierarchical mesoporous perovskite $La_{0.5}Sr_{0.5}CoO_{2.91}$ (LSCO) nanowires. We tested the intrinsic oxygen reduction reaction (ORR) and oxygen evolution reaction (OER) activity in both aqueous electrolytes and nonaqueous electrolytes via rotating disk electrode (RDE) measurements and demonstrated that the hierarchical mesoporous LSCO nanowires are high-performance catalysts for the ORR with low peak-up potential and high limiting diffusion current. Furthermore, we fabricated Li-air batteries on the basis of hierarchical mesoporous LSCO nanowires and nonaqueous electrolytes, which exhibited ultrahigh capacity, ca. over 11,000 mAh·g^{-1}, one order of magnitude higher than that of LSCO nanoparticles. Besides, the possible reaction mechanism is proposed to explain the catalytic activity of the LSCO mesoporous nanowire.

electrocatalysis | energy storage

With the growth of energy demand, searching for new clean energy sources to replace conventional fuel energy has been a challenge today (1–6). Li-ion batteries have developed rapidly in recent years because of their low cost, long cycle life, good reversibility, and no memory effect. However, even when it was fully developed, the highest energy storage of Li-ion batteries is insufficient to satisfy the ever-increasing requirements for batteries with high capacities (7, 8). Recently, Li-air batteries have attracted great interest because they potentially have much higher gravimetric energy storage density compared with all other chemical batteries (9–18). They could theoretically offer very high specific energies (i.e., 5,000 Wh·kg^{-1}) because oxygen, the cathode active material, is not stored in the battery, but can be accessed from the environment. Thus, Li-air batteries are eco-friendly electrochemical power sources.

However, there are some challenges in Li-air battery research. In an aprotic electrolyte, the fundamental cathode discharge reactions are thought to be $2Li + O_2 \rightarrow Li_2O_2$ and $2Li + 0.5O_2 \rightarrow Li_2O$. Recent studies demonstrated the degradation of the electrolyte (19, 20), and the precipitation of reaction products Li_2O_2/Li_2O or electrolyte decomposition products on the catalyst and electrode eventually blocked the oxygen pathway and limited the capacity of the Li-air batteries.

To enhance the performance, it has been suggested that one method for enhancing the mobility of oxygen ions is to provide disorder-free channels of oxygen vacancies, using compounds with the perovskite structure that exhibits cation ordering (21, 22). It is well known that perovskite materials have wide applications in catalysis for fuel cells and metal–air batteries due to their defective structures and excellent oxygen mobility. Shao-Horn and coworkers have deeply studied perovskite oxides for oxygen evolution reaction (OER) catalysis and found that $Ba_{0.5}Sr_{0.5}Co_{0.8}Fe_{0.2}O_{3-x}$ and $La_{0.5}Ca_{0.5}CoO_{3-x}$ catalyze the OER with intrinsic activity that is at least an order of magnitude higher than that of the state-of-the-art iridium oxide catalyst in alkaline media (21). Another method of increasing the oxygen pathway is using porous structure (20, 23–26). Wu et al. have synthesized highly ordered mesoporous platinum@graphitic carbon composites as an oxygen reduction electrocatalyst that exhibited much higher active capacity for Li-air batteries (24).

$La_{0.5}Sr_{0.5}CoO_{3-\delta}$ (LSCO) has been considered one of the best candidates for cathode materials in solid oxide fuel cells (SOFCs) and as a catalyst in Li-air batteries (22, 27–32). In this paper, hierarchical perovskite LSCO mesoporous nanowires were synthesized using a facile multistep microemulsion with $La(NO_3)_3$, $Sr(NO_3)_2$, $Co(NO_3)_2$, and KOH followed by a slow annealing method. As a control experiment, LSCO nanoparticles were also synthesized by a similar method but rapid annealing was used (Fig. S1 shows details of the synthesis and reaction; Fig. S2 shows a control experiment).

To determine the phase structures of the products, the X-ray diffraction (XRD) measurements were conducted. Reaction products before slow annealing [▲, peaks of $La_{0.5}Sr_{0.5}CoO_{2.91}$; △, peaks of $La(OH)_3$; ●, peaks of $Co(OH)_2$; and ○, peaks of $Sr(OH)_2{\cdot}8H_2O$] are identified in Fig. S3. After slow annealing, the XRD patterns of the nanowires (Fig. 1*A*) exhibit consistent diffraction peaks with those of the $La_{0.5}Sr_{0.5}CoO_{2.91}$ (JCPDS card no. 00-048-0122: a = 5.4300 Å, b = 5.4300 Å, c = 13.2516 Å), indicating the pure phase of these nanowires. A model of the LSCO (Fig. 1*A*, *Inset*) shows a typical perovskite structure and oxygen vacancies in which ionic transport can be enhanced. A more accurate model of the LSCO structure and an explanation are shown in Fig. S4 (28). It is well known that perovskite materials have wide applications in catalysis due to their defective structures and excellent oxygen mobility. Meanwhile, more disorder-free channels can be obtained from the crystal structure of perovskite $La_{0.5}Sr_{0.5}CoO_{2.91}$. A significant disorder exists between the La and Sr layers. Thus, oxygen can diffuse easily and be stored in and between the crystal lattice structures.

Scanning electron microscopy (SEM) and transmission electron microscopy (TEM) techniques were further used to characterize the morphology and detailed structure of the products. As can be seen from the SEM image (Fig. 1*C*), the as-prepared hierarchical mesoporous LSCO nanowire with diameter around 150 nm is composed of interconnected nanorods, and the surface is rough and porous. Further information about the hierarchical LSCO mesoporous nanowire was obtained from a TEM image (Fig. 1 *D* and *E*). It is confirmed that the nanorods have diameters of about 40 nm. From Fig. 1*E*, *Inset*, the pores in LSCO nanorods from the mesoporous nanowire were observed; another clear image is also shown in Fig. S5. Close inspection at the junction shows that the LSCO nanorods were orientedly collected, suggesting that the LSCO nanorods were not just loosely attached. The high-resolution (HR)TEM image at the junction (Fig. 1*F*) shows that LSCO nanorods are tightly attached to each other at an atomic level when they formed the hierarchical nanowire. This unique structure provides good physical contact between the nanorods and an increased oxygen pathway and is beneficial for electronic conduction.

Author contributions: Y.Z. and L.M. designed research; Y.Z. and X.L. performed research; Y.Z. and L.X. contributed new reagents/analytic tools; Y.Z., L.X., C.H., Q.A., X.X., and Q.Z. analyzed data; and Y.Z., L.X., and L.M. wrote the paper.

The authors declare no conflict of interest.

*This Direct Submission article had a prearranged editor.

[1]Y.Z. and L.X. contributed equally to this work.

[2]To whom correspondence should be addressed. E-mail: mlq518@whut.edu.cn.

This article contains supporting information online at www.pnas.org/lookup/suppl/doi:10.1073/pnas.1210315109/-/DCSupplemental.

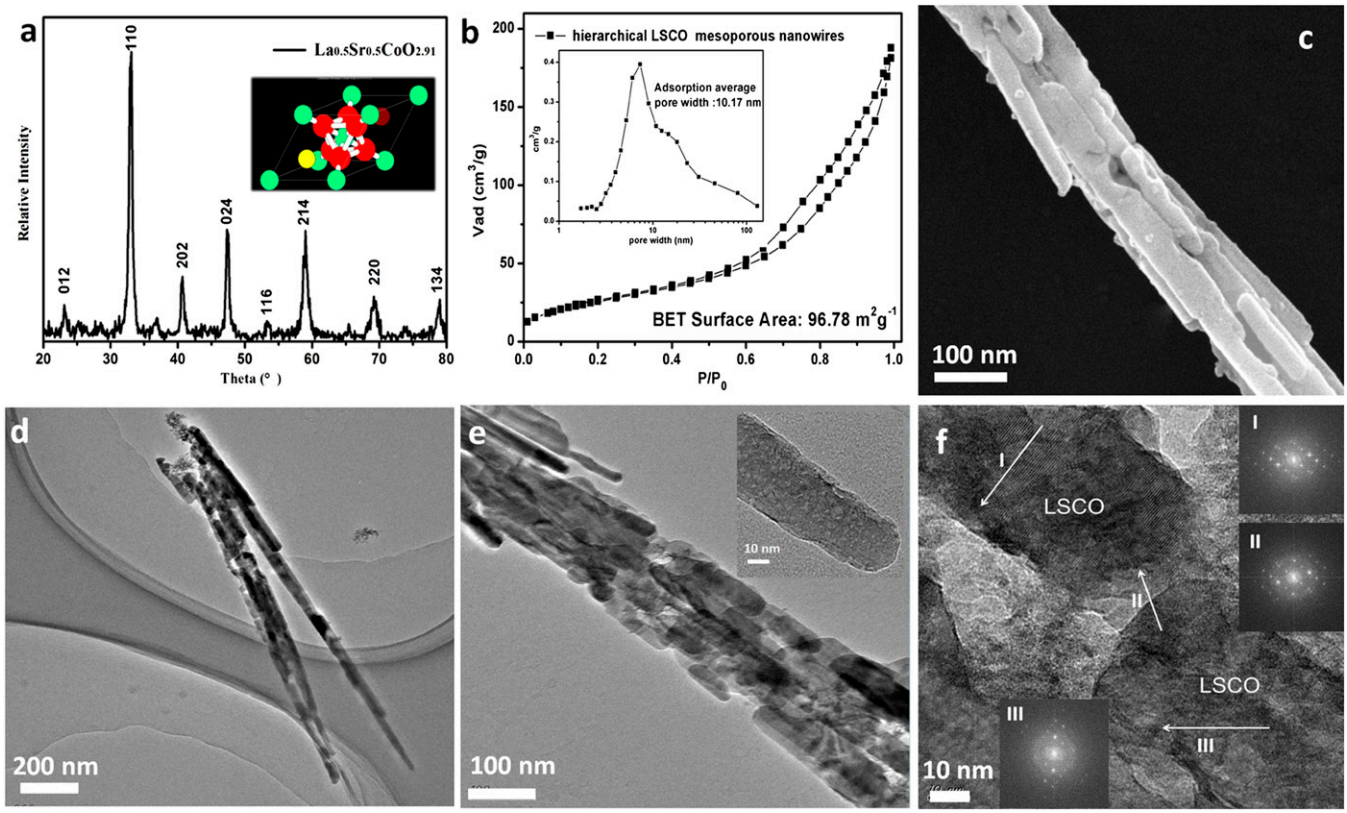

Fig. 1. Phase analysis and morphology characterization. (*A*) XRD pattern of hierarchical mesoporous LSCO nanowires after annealing. (*Inset* shows a model of the perovskite structure LSCO. Green balls represent Co atoms; red balls, O atoms; yellow ball, a La atom; and wine ball, a Sr atom. One of the apical oxygen sites is vacated and the unit cell is doubled.) (*B*) Nitrogen adsorption and desorption isotherms and pore size distribution (*Inset*) of hierarchical mesoporous LSCO nanowires after annealing. (*C*) SEM image of the hierarchical mesoporous LSCO nanowires. (*D* and *E*) TEM and HRTEM images of the hierarchical mesoporous LSCO nanowires (*Inset* shows porous LSCO nanorods from mesoporous nanowires). (*F*) HRTEM image at the junction of mesoporous LSCO nanowires and FFT patterns on selected areas. The arrows represent crystal lattice direction.

Remarkably, from the arrows and fast Fourier transform (FFT) patterns on selected areas (Fig. 1*F*), the crystal directions of LSCO internal crystal and external junction are different, which demonstrates that the LSCO nanorod and hierarchical nanowire crystallization are not simultaneous. The possible formation mechanism for the hierarchical mesoporous LSCO nanowires is suggested, as shown in Fig. 2. In the process of preparing hierarchical mesoporous LSCO nanowires, LSCO nanorods first crystallize and grow in the microemulsion of $La(NO_3)_3$, $Sr(NO_3)_2$, $Co(NO_3)_2$, and KOH at a high stirring rate (SEM image in Fig. S6*A*). Then LSCO nanorods self-assemble at a low stirring rate and a bigger water pool in microemulsion, and then LSCO nanorods play the role of a template itself for the oriented growth of attached nanorods, which results in the formation of hierarchical mesoporous LSCO nanowires.

The N_2 adsorption desorption isotherms and the corresponding Barrett–Joyner–Halenda (BJH) pore-size distributions are shown in Fig. 1*B*. The hierarchical mesoporous LSCO nanowires present typical type-IV N_2 sorption isotherms with distinct H3 hysteresis loops that can be linked to slit-shaped pores. The pore-size distribution curve shows consequent mesoporous nanowires with an average pore width ~10.17 nm. The specific surface area of mesoporous nanowires is 96.78 m^2/g, which is much larger than that of reported nanowires with similar size (27). Remarkably, these kinds of unique pores can effectively provide disorder-free channels of oxygen vacancies that may improve the electrocatalytic performance and Li-air battery performance.

Results and Discussion

The efficiency of Li-air batteries, to some extent, is limited by the slow kinetics of the oxygen reduction reaction (ORR) and the OER (22, 33–43). To assess their ORR and OER catalytic activity, our materials were first loaded (with the same mass loading) onto glassy carbon electrodes. We used rotating-disk electrode (RDE) measurements to reveal the ORR kinetics of catalyst in aqueous elec-

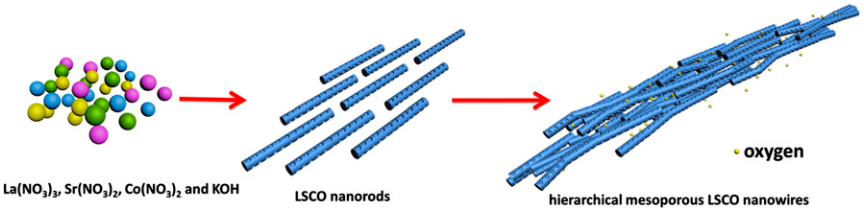

Fig. 2. The schematic model diagram of constructing hierarchical mesoporous LSCO nanowires.

trolyte, in 0.1 M KOH (Fig. 3). Fig. 3*A* shows the cyclic voltammogram of activated carbon (AC), LSCO nanoparticles + AC, and hierarchical mesoporous LSCO nanowires + AC electrode in O_2-saturated 0.1 M KOH at a scan rate of 5 mV·s^{-1} in the range of 0.4–1.0 V reversible hydrogen electrode (RHE) ($r = 0$ rpm). The cyclic voltammetry (CV) curve of hierarchical mesoporous LSCO nanowires + AC exhibit more positive ORR peak potential and higher peak current than AC and LSCO nanoparticles + AC. Fig. 3 *B–D* shows the linear scanning voltammograms of the catalyst-coated RDE obtained under various rotating speeds from 400 to 2,000 rpm. The half-wave potential at 1,600 rpm was ~0.77 V (Fig. 3*D*), more positive than that of AC (~0.62 V; Fig. 3*C*) and LSCO nanoparticles + AC (~0.67 V; Fig. 3*D*). Excellently, the limiting diffusion current of hierarchical mesoporous LSCO nanowires + AC electrode can reach to −13 mA·cm^{-2}, which is much higher than that of activated carbon or other catalysts for Li-air batteries. The equation

$$\frac{1}{i} = \frac{1}{i_k} + \frac{1}{i_d} = \frac{1}{nFAkC^o} - \frac{1}{0.62nFAD_{O_2}^{2/3}v^{-1/6}C^o\omega^{1/2}}, \quad [1]$$

where i (shown in Eq. **1**, above) corresponds to the measured current, n is the overall transferred electron number, F is the Faraday constant, C^0 is the saturated concentration of oxygen in 0.1 M KOH (1.14×10^{-6} mol·cm^{-3}), A is the geometric area of the electrode (cm^2), ω is the rotating rate (rad·s^{-1}), D_{O_2} is the diffusion coefficient of oxygen (1.73×10^{-5} cm^2·s^{-1}), v is the kinetic viscosity of the solution (0.01 cm^2·s^{-1}), and k is the rate constant for oxygen reduction, is widely used to analyze the ORR reaction kinetics. The Koutecky–Levich plot is shown in Fig. 3*E*. On the basis of the average values calculated from different potentials, overall electron transfer numbers of AC, LSCO nanoparticles + AC, and hierarchical mesoporous LSCO nanowires + AC are, respectively, 2.2, 3.0, and 3.1. And the overall electron transfer number of hierarchical mesoporous LSCO nanowires + AC ($n = 3.1$) is quite close to pure α-MnO_2 ($n = 3.1$) for the ORR in alkaline solution (34). Attractively, the hierarchical mesoporous LSCO nanowires and LSCO nanoparticles have a similar overall electron transfer number (3.1 vs. 3.0), but hierarchical mesoporous nanowires have a high limiting diffusion current, which indicates that the hierarchical mesoporous nanostructure can provide surface active sites for oxygen reduction reaction and possess sufficient order to enable O_2 access to the heterostructures facilely. Fig. 3*F* shows that as the catalyst for a Li-air battery, mesoporous LSCO nanowires have better ORR and OER activity.

To further study the catalytic performance in a nonaqueous electrolyte, CV and ORR/OER polarization curves were tested in a nonaqueous electrolyte from 4.2 V to 2 V (V vs. Li) by RDE, with the same electrolyte, electrode, and potential region as those in Li-air batteries, shown in Fig. 4. The CV and ORR/OER polarization curves of hierarchical mesoporous LSCO nanowires + AC exhibit more positive ORR peak potential (~2.9 V), and higher peak current than those of AC and LSCO nanoparticles + AC.

To investigate their electrochemical performances, we fabricated Li-air batteries in a nonaqueous electrolyte. Distinct from others, the catalyst inks were dispersed on a pretreated filter

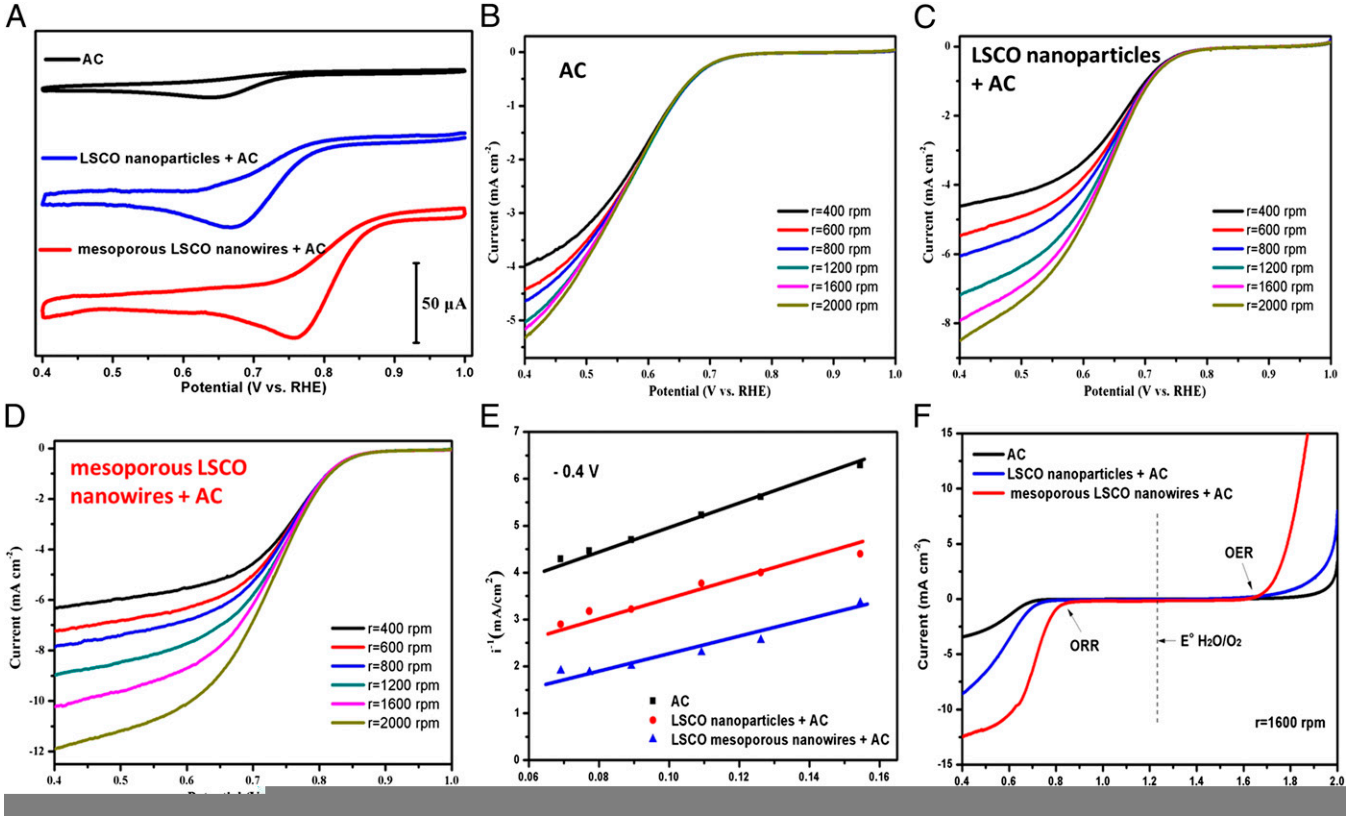

Fig. 3. Oxygen reduction and oxygen evolution catalytic performance on glassy carbon electrodes in O_2 saturated in aqueous electrolyte, 0.1 M KOH with a sweep rate of 5 mV·s^{-1}. (*A*) CV curves of activated carbon (AC), LSCO nanoparticles + AC, and hierarchical mesoporous LSCO nanowires + AC. (*B–D*) ORR polarization curves of AC, LSCO nanoparticles + AC, and hierarchical mesoporous LSCO nanowires + AC at different rotation rates. (*E*) Koutecky–Levich plot based on ORR polarization curves at −0.4 V. (*F*) ORR and OER polarization curves of AC, LSCO nanoparticles + AC, and hierarchical mesoporous LSCO nanowires + AC on glassy carbon electrodes at 1,600-rpm rotation rates.

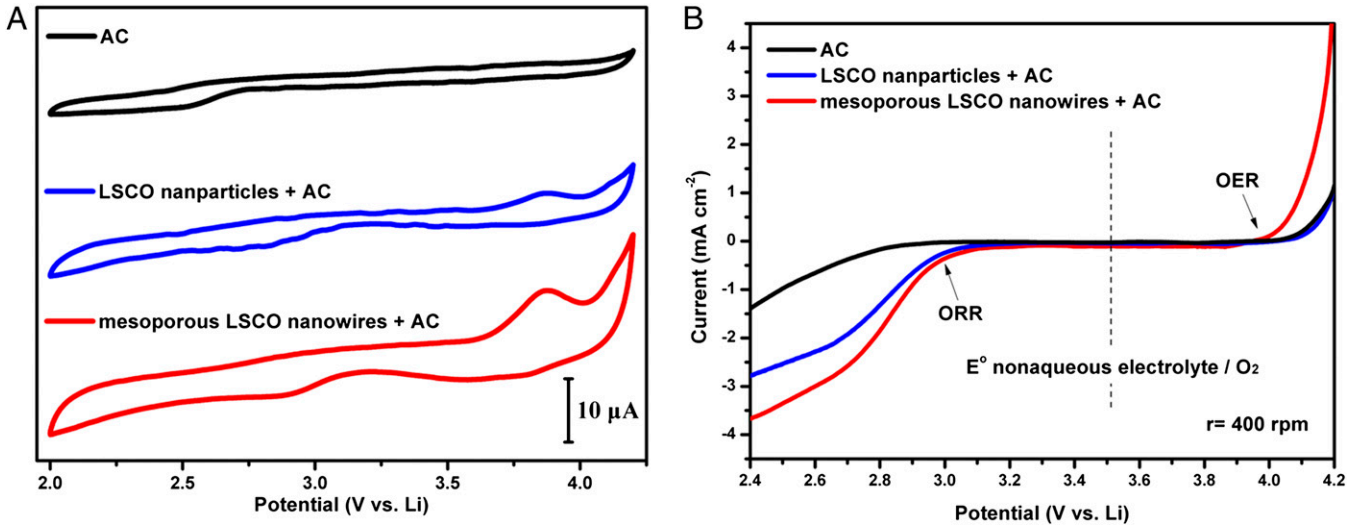

Fig. 4. Oxygen reduction and oxygen evolution catalytic performance on glassy carbon electrodes in O_2 saturated in nonaqueous electrolyte with a sweep rate of 5 mV·s^{-1}. Lithium metal was used as a counterelectrode. (*A*) CV curves of AC, LSCO nanoparticles + AC, and hierarchical mesoporous LSCO nanowires + AC. (*B*) ORR and OER polarization curves of AC, LSCO nanoparticles + AC, and hierarchical mesoporous LSCO nanowires + AC on glassy carbon electrodes at 400-rpm rotation rates.

paper that can provide plenty of oxygen channels, load reaction products, and protect anode and electrolyte from H_2O to some extent (Fig. S8*A*). Fig. 5 shows the discharge curve of Li-air batteries, using a filter paper-supported nanocrystals electrode tested in the ambient environment by the addition of oxygen (oxygen pressure close to 1 atm) or argon. It was tested under the current density 50 mA/g, including the mass of LSCO nanomaterial and AC from 2 V to 4.2 V. To exclude possible electrochemical contributions from the lithium intercalation/deintercalation or nonoxidative effect of decomposition of organic functional, the electrode was discharged to 2.0 V in pure argon as shown in Fig. 5*A*. The discharge capacity of hierarchical mesoporous LSCO nanowires + AC testing in pure argon is limited to 42 mAh/g. However, the capacity has greatly increased under oxygen, shown in Fig. 5 *B–D*. Surprisingly, the discharge capacity of perovskite LSCO mesoporous nanowires + AC electrodes can reach 11,059 mAh/g with a plateau at around 2.7 V and the corresponding specific energy is 27,647 Wh/kg, with an average voltage of 2.5 V. The capacity of LSCO mesoporous nanowires + AC electrodes is significantly higher than that of activated carbon (1,444 mAh/g) and LSCO nanoparticles + AC (5,302

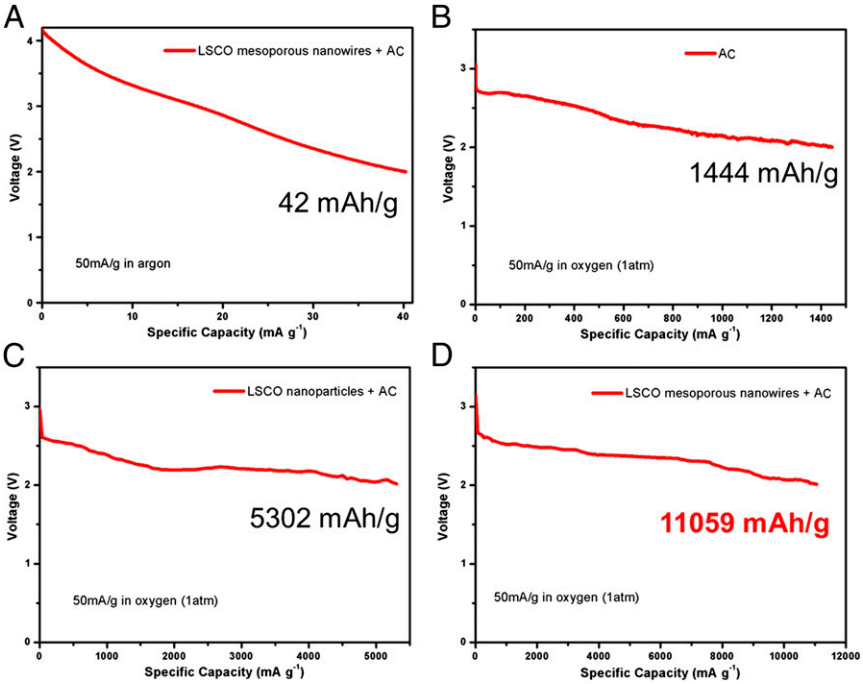

Fig. 5. Electrochemical performances of Li-air batteries. (*A*) The discharge curve of Li-air batteries using hierarchical mesoporous LSCO nanowires + AC as the air electrode in the pure argon atmosphere. (*B–D*) The discharge curve of Li-air batteries using AC, LSCO nanoparticles + AC, and hierarchical mesoporous LSCO nanowires + AC as the air electrode in oxygen (Po_2 = 1 atm).

mA/g). The hysteresis tested by RDE shown in Fig. 4 is ~2.9 V whereas the plateau in the Li-air batteries test is ~2.7 V. Considering the resistance voltage drop caused by the battery separator or pretreated filter paper, the result here is reasonable.

To explain the electrochemical results, it is important to consider the hierarchical perovskite mesoporous structure that exerts such a significant influence on discharge capacity. Here, there are four possible factors to affect the enhanced discharge capacity in Li-air batteries. First, this performance is related to the Brunauer–Emmet–Teller (BET) surface area. The BET surface area of LSCO mesoporous nanowires reaches 96.78 $m^2 \cdot g^{-1}$, which is much larger than that of the prepared LSCO nanoparticles (11.87 $m^2 \cdot g^{-1}$) (Fig. S2*C*) and other nanowires with similar size as reported. Second, the continuous disorder-piled pores formed by attached LSCO nanorods are able to provide free channels for oxygen even when the reaction products Li_2O_2/Li_2O or electrolyte decomposition products cover the surface of catalyst and electrode. Third, perovskite-defective structures and small pores on the LSCO nanorods strongly increase oxygen mobility at a lower scale and the kinetics of the oxygen reduction reaction. Fourth, this kind of hierarchical structure shows that the self-aggregation of nanorods was greatly reduced because of the attachment of nanorods in the nanowires, which provides more active sites and keeps the surface area large to make full use of the advantages of nanostructured materials.

Although the Li-air batteries have ultrahigh capacity and specific energy, there are numerous scientific challenges to be overcome. To further study the reaction mechanism of Li-air batteries and the LSCO catalyst effect, here we disassembled the batteries and analyzed the anode and cathode materials before and after discharge, which is shown in Figs. S7 and S8. At the anode, the metal Li foil before discharge is a bright and metallic color. However, the metal Li foil surface after discharge in an ambient environment turned into off-white. The XRD indicates that the white materials are a mixture of $LiOH \cdot H_2O$, LiOH, and electrolyte decomposition products, which may influence the cycling performance of the Li-air battery. At the cathode side, the size of catalysts has increased due to ORR or electrolyte decomposition products covering the surface of the catalyst and electrode, as shown in Fig. S8.

To explain the catalytic activity of the LSCO mesoporous nanowire, a possible mechanism was proposed by considering the structure of perovskite and the reaction path of O_2 reduction. Recently, Bruce et al. (10) demonstrated that LiO_2 is an intermediate on O_2 reduction in a nonaqueous Li-O_2 battery and Li-air battery reactions were given as follows:

$$O_2 + e^- \rightarrow O_2^- \quad [2]$$

$$O_2^- + Li^+ \rightarrow LiO_2 \quad [3]$$

$$2LiO_2 \rightarrow Li_2O_2 + O_2. \quad [4]$$

Considering that O_2^- has a high activity and LiO_2 is not stable, Eq. **2** is the rate-controlling step. In our work, Fig. 4 shows that the CV and ORR/OER polarization curves of hierarchical mesoporous LSCO nanowires exhibited a more positive ORR peak potential and higher peak current than AC and LSCO nanoparticles. We suppose that the hierarchical mesoporous LSCO perovskite structure makes the ORR reaction (Eq. **2**) easier and more rapid and the possible reason is as follows.

In Eq. **2**, influence factors include oxygen diffusion, oxygen chemisorption, and O_2^- desorption. Because of its 1D mesoporous structure and oxygen vacancies, LSCO provides enough free channels for oxygen diffusion. Meanwhile, according to molecular orbital principles (21), O_2 and Co ions may be functionally similar to Lewis acid and Lewis base sites, respectively. Here, Co ions can act as an active center for O_2 chemisorption. CoO_6 species with e_g electrons can donate electrons to σ^*2p orbitals of O_2. The t_{2g} electrons of Co ions can interact with π^*2p electrons of O_2 to form a π-bond. Thus, the bond (Co-O_2) strength and oxygen chemisorption can be increased. Additionally, oxygen vacancies in the LSCO catalyst can decrease the repulsion between adsorbed O and lattice O, leading to enhanced oxygen chemisorption. The high specific surface area, perovskite structure, and mesoporous structure of LSCO are beneficial to Li^+ diffusion and the formation rate of LiO_2 and Li_2O_2.

In summary, a facile multistep microemulsion followed by a slow annealing method was used to fabricate hierarchical perovskite $La_{0.5}Sr_{0.5}CoO_{2.91}$ mesoporous nanowires and we demonstrate that the hierarchical mesoporous LSCO nanowires are high-performance catalysts for the ORR with low peak-up potential and high limiting diffusion current. The specific capacity of the Li-air battery based on hierarchical mesoporous LSCO nanowires is over 11,000 $mAh \cdot g^{-1}$, which exhibits ultrahigh performance for the Li-air battery. Besides, the possible reaction mechanism is proposed to explain the catalytic activity and Li-air batteries reactions. The hierarchical perovskite mesoporous $La_{0.5}Sr_{0.5}CoO_{2.91}$ described in this article will have great potential applications in the Li-air battery, fuel cells, or other electrochemical devices.

Materials and Methods

Materials Synthesis. Hierarchical mesoporous perovskite LSCO nanowires were synthesized using a facile multistep microemulsion with $La(NO_3)_3$, $Sr(NO_3)_2$, $Co(NO_3)_2$, and KOH, which was followed by vigorous stirring and then slow stirring for 6 h at room temperature and aging for 24 h after demulsification. The nanowires were then annealed at 800 °C at the rate of 1 °C/min in argon gas to obtain hierarchical perovskite $La_{0.5}Sr_{0.5}CoO_{2.91}$ mesoporous nanowires. As a control experiment, LSCO nanoparticles were also synthesized by a similar proportion but rapid annealing was used (10 °C/min) (synthesis details in Fig. S1).

Electrochemical Measurements. Five milligrams of AC (XC-72) or 0.75 mg of LSCO nanoparticles mixed with 4.25 mg of AC or 0.75 mg hierarchical mesoporous LSCO nanowires mixed with 4.25 mg AC and 122 μL of 5 wt% Nafion solutions were dispersed in 1 mL of 3:1 vol/vol water/isopropanol mixed solvent by at least 30 min sonication to form a homogeneous ink. A saturated calomel electrode was used as the reference electrode in all measurements and was calibrated with respect to a reversible hydrogen electrode. Cyclic voltammetry and linear scanning voltammetry were conducted in a three-electrode electrochemical cell. Twenty micrograms of sample was loaded on the glassy carbon working electrode (5 mm in diameter). Electrochemical data were collected with an Autolab electrochemical workstation. KOH (0.1 M) and $LiPF_6$ (1 M) in ethylene carbon/dimethyl carbonate were used as the electrolyte. The three-electrode cell used for RDE measurements (Pine) consists of a platinum electrode as a counterelectrode, a saturated calomel electrode as a reference electrode or a lithium-foil counterelectrode, and a platinum electrode as a reference electrode. For the measurement on filter paper, the working electrode was prepared by loading 2 mg of sample from its ink. The electrochemical properties were carried out by assembling 2,025 coin cells in a glove box filled with pure argon gas, using a lithium pellet as the anode, 1 M solution of $LiPF_6$ in ethylene carbon (EC)/dimethyl carbonate (DMC) as the electrolyte, and filter paper-supported samples as cathode electrodes. Galvanostatic discharge was studied in a potential range of 4.2–2.0 V vs. Li/Li^+ with a multichannel battery testing system (LAND CT 2001A).

Characterization. The crystal phase and purity of the products were characterized by X-ray powder diffraction. X-ray diffraction patterns of the products were recorded on a Rigaku D/MAX-III diffractometer with monochromatized Cu K_a radiation (k = 1.5406 Å). Field-emission scanning electron microscopy images were collected with a Hitachi S-4800 at an acceleration voltage of 10 kV. TEM and HRTEM images were recorded by using a JEOL JEM-2010 FEF microscope at an accelerating voltage of 200 kV. Energy dispersive spectroscopy (EDS) was performed on a JEM 2100F STEM/EDS. Nitrogen adsorption and desorption isotherms were measured using a Gemini 2360 instrument by adsorption of nitrogen at −209 °C.

ACKNOWLEDGMENTS. This work was supported by the National Basic Research Program of China (2013CB934103, 2012CB933003), the National Natural Science Foundation of China (51272197 and 51072153), the International S&T Cooperation (2013ZR02930), the Program for New Century Excellent Talents in University (NCET-10-0661), and the Fundamental Research Funds for the Central Universities (2011-II-012).

1. Armand M, Tarascon JM (2008) Building better batteries. *Nature* 451(7179):652–657.
2. Dunn B, Kamath H, Tarascon JM (2011) Electrical energy storage for the grid: A battery of choices. *Science* 334(6058):928–935.
3. Bruce PG, Scrosati B, Tarascon JM (2008) Nanomaterials for rechargeable lithium batteries. *Angew Chem Int Ed Engl* 47(16):2930–2946.
4. Mai LQ, et al. (2011) Hierarchical $MnMoO_{(4)}$/$CoMoO_{(4)}$ heterostructured nanowires with enhanced supercapacitor performance. *Nat Commun* 2:381.
5. Tian B, Kempa TJ, Lieber CM (2009) Single nanowire photovoltaics. *Chem Soc Rev* 38 (1):16–24.
6. Kempa TJ, et al. (2012) Coaxial multishell nanowires with high-quality electronic interfaces and tunable optical cavities for ultrathin photovoltaics. *Proc Natl Acad Sci USA* 109(5):1407–1412.
7. Goodenough JB, Kim Y (2009) Challenges for rechargeable Li batteries. *Chem Mater* 22:587–603.
8. Tarascon JM, Armand M (2001) Issues and challenges facing rechargeable lithium batteries. *Nature* 414(6861):359–367.
9. Abraham K, Jiang Z (1996) A Polymer electrolyte-based rechargeable lithium/oxygen battery. *J Electrochem Soc* 143:1–5.
10. Bruce PG, Freunberger SA, Hardwick LJ, Tarascon JM (2012) Li-O_2 and Li-S batteries with high energy storage. *Nat Mater* 11(1):19–29.
11. Cui Y, Wen Z, Liu Y (2011) A free-standing-type design for cathodes of rechargeable Li-O_2 batteries. *Energy Environ Sci* 4:4727–4734.
12. Suntivich J, et al. (2011) Design principles for oxygen-reduction activity on perovskite oxide catalysts for fuel cells and metal-air batteries. *Nat Chem* 3(7):546–550.
13. Kraytsberg A, Ein-Eli Y (2011) Review on Li-air batteries-opportunities, limitations and perspective. *J Power Sources* 196:886–893.
14. Jung HG, Hassoun J, Park JB, Sun YK, Scrosati B (2012) An improved high-performance lithium-air battery. *Nat Chem* 4(7):579–585.
15. Peng Z, Freunberger SA, Chen Y, Bruce PG (2012) A reversible and higher-rate Li-O_2 battery. *Science* 337(6094):563–566.
16. Lu YC, et al. (2010) Platinum-gold nanoparticles: A highly active bifunctional electrocatalyst for rechargeable lithium-air batteries. *J Am Chem Soc* 132(35): 12170–12171.
17. Veith GM, Dudney NJ (2011) Current collectors for rechargeable Li-air batteries. *J Electrochem Soc* 158:A658–A663.
18. Xiao J, et al. (2011) Hierarchically porous graphene as a lithium-air battery electrode. *Nano Lett* 11(11):5071–5078.
19. Freunberger SA, et al. (2011) Reactions in the rechargeable lithium-O_2 battery with alkyl carbonate electrolytes. *J Am Chem Soc* 133(20):8040–8047.
20. Xiao J, et al. (2010) Optimization of air electrode for Li/air batteries. *J Electrochem Soc* 157:A487–A492.
21. Suntivich J, May KJ, Gasteiger HA, Goodenough JB, Shao-Horn Y (2011) A perovskite oxide optimized for oxygen evolution catalysis from molecular orbital principles. *Science* 334(6061):1383–1385.
22. Suntivich J, Gasteiger HA, Yabuuchi N, Shao-Horn Y (2010) Electrocatalytic measurement methodology of oxide catalysts using a thin-film rotating disk electrode. *J Electrochem Soc* 157:B1263–B1268.
23. Mirzaeian M, Hall PJ (2009) Preparation of controlled porosity carbon aerogels for energy storage in rechargeable lithium oxygen batteries. *Electrochim Acta* 54: 7444–7451.
24. Wu Z, Lv Y, Xia Y, Webley PA, Zhao D (2012) Ordered mesoporous platinum@-graphitic carbon embedded nanophase as a highly active, stable, and methanol-tolerant oxygen reduction electrocatalyst. *J Am Chem Soc* 134(4):2236–2245.
25. Zhou L, Zhao D, Lou XW (2012) Double-shelled $CoMn_2O_4$ hollow microcubes as high-capacity anodes for lithium-ion batteries. *Adv Mater (Deerfield Beach Fla)* 24(6): 745–748.
26. Mai LQ, et al. (2010) Electrospun ultralong hierarchical vanadium oxide nanowires with high performance for lithium ion batteries. *Nano Lett* 10(11):4750–4755.
27. Deng J, Zhang L, Dai H, He H, Au CT (2008) Single-crystalline $La_{0.6}Sr_{0.4}CoO_{3-\delta}$ nanowires/nanorods derived hydrothermally without the use of a template: Catalysts highly active for toluene complete oxidation. *Catal Lett* 123:294–300.
28. Donner W, et al. (2011) Epitaxial strain-induced chemical ordering in $La_{0.5}Sr_{0.5}CoO_{3-\delta}$ films on $SrTiO_3$. *Chem Mater* 23:984–988.
29. Li WW, et al. (2010) Growth, microstructure, and infrared-ultraviolet optical conductivity of $La_{(0.5)}Sr_{(0.5)}CoO_{(3)}$ nanocrystalline films on silicon substrates by pulsed laser deposition. *ACS Appl Mater Interfaces* 2(3):896–902.
30. Liu W, et al. (2008) $La_{0.5}Sr_{0.5}CoO_{3-\delta}$ nanotubes sensor for room temperature detection of ammonia. *Sens Actuators B Chem* 134:62–65.
31. Yu HC, Fung KZ, Guo TC, Chang WL (2004) Syntheses of perovskite oxides nanoparticles $La_{1-x}Sr_xMO_{3-\delta}$ (M = Co and Cu) as anode electrocatalyst for direct methanol fuel cell. *Electrochim Acta* 50(2–3):811–816.
32. Wang Y, Fan HJ (2010) Improved thermoelectric properties of $La_{1-x}Sr_xCoO_3$ nanowires. *J Phys Chem C* 114:13947–13953.
33. Byon HR, Suntivich J, Shao-Horn Y (2011) Graphene-based non-noble-metal catalysts for oxygen reduction reaction in acid. *Chem Mater* 23:3421–3428.
34. Cheng F, Su Y, Liang J, Tao Z, Chen J (2009) MnO_2-based nanostructures as catalysts for electrochemical oxygen reduction in alkaline media. *Chem Mater* 22:898–905.
35. Débart A, Bao J, Armstrong G, Bruce PG (2007) An O_2 cathode for rechargeable lithium batteries: The effect of a catalyst. *J Power Sources* 174:1177–1182.
36. Liang Y, et al. (2011) Co_3O_4 nanocrystals on graphene as a synergistic catalyst for oxygen reduction reaction. *Nat Mater* 10(10):780–786.
37. Lim B, et al. (2009) Pd-Pt bimetallic nanodendrites with high activity for oxygen reduction. *Science* 324(5932):1302–1305.
38. Lu YC, Gasteiger HA, Parent MC, Chiloyan V, Shao-Horn Y (2010) The influence of catalysts on discharge and charge voltages of rechargeable Li–oxygen batteries. *Electrochem Solid-State Lett* 13:A69–A72.
39. Lu YC, Gasteiger HA, Shao-Horn Y (2011) Method development to evaluate the oxygen reduction activity of high-surface-area catalysts for Li-air batteries. *Electrochem Solid-State Lett* 14:A70–A74.
40. Lu YC, Gasteiger HA, Shao-Horn Y (2011) Catalytic activity trends of oxygen reduction reaction for nonaqueous Li-air batteries. *J Am Chem Soc* 133(47):19048–19051.
41. Yin F, Takanabe K, Katayama M, Kubota J, Domen K (2010) Improved catalytic performance of nitrided Co-Ti and Fe-Ti catalysts for oxygen reduction as non-noble metal cathodes in acidic media. *Electrochem Commun* 12:1177–1179.
42. Cheng F, et al. (2011) Rapid room-temperature synthesis of nanocrystalline spinels as oxygen reduction and evolution electrocatalysts. *Nat Chem* 3(1):79–84.
43. Wang L, et al. (2011) $CoMn_2O_4$ spinel nanoparticles grown on graphene as bifunctional catalyst for lithium-air batteries. *J Electrochem Soc* 158:A1379–A1382.